PHYSICAL REVIEW D **84,** 054506 (2011)

Two-nucleon bound states in quenched lattice QCD

T. Yamazaki,[1,2] Y. Kuramashi,[2,3,4] and A. Ukawa[2]

(PACS-CS Collaboration)

[1]*Kobayashi-Maskawa Institute for the Origin of Particles and the Universe, Nagoya University, Naogya, Aichi 464-8602, Japan*
[2]*Center for Computational Sciences, University of Tsukuba, Tsukuba, Ibaraki 305-8577, Japan*
[3]*Graduate School of Pure and Applied Sciences, University of Tsukuba, Tsukuba, Ibaraki 305-8571, Japan*
[4]*RIKEN Advanced Institute for Computational Science, Kobe, Hyogo 650-0047, Japan*
(Received 10 May 2011; published 21 September 2011)

We address the issue of bound state in the two-nucleon system in lattice QCD. Our study is made in the quenched approximation at the lattice spacing of $a = 0.128$ fm with a heavy quark mass corresponding to $m_\pi = 0.8$ GeV. To distinguish a bound state from an attractive scattering state, we investigate the volume dependence of the energy difference between the ground state and the free two-nucleon state by changing the spatial extent of the lattice from 3.1 fm to 12.3 fm. A finite energy difference left in the infinite spatial volume limit leads us to the conclusion that the measured ground states for not only spin triplet but also singlet channels are bounded. Furthermore the existence of the bound state is confirmed by investigating the properties of the energy for the first excited state obtained by a 2×2 diagonalization method. The scattering lengths for both channels are evaluated by applying the finite volume formula derived by Lüscher to the energy of the first excited states.

DOI: 10.1103/PhysRevD.84.054506 PACS numbers: 11.15.Ha, 12.38.−t, 12.38.Aw, 12.38.Gc

I. INTRODUCTION

The strong interaction dynamically generates a hierarchical structure: three quarks are bound to form a nucleon with an energy of 1 GeV, and nucleons are in turn bound to form nuclei with a binding energy of 10 MeV or so per nucleon. This is a multiscale physics that computational physics should explore, and lattice QCD is responsible for explaining the nature of nuclei based on first principles.

Recently, the present authors have made a first attempt to directly construct the helium-3 and helium-4 nuclei from quarks and gluons in lattice QCD. In order to control statistical errors in the Monte Carlo evaluation of the helium Green's function, as well as quark contractions whose number factorially increases with the nuclear mass number, calculations were carried out at a rather heavy degenerate up- and down-quark mass corresponding to $m_\pi = 0.8$ GeV in quenched QCD [1]. We successfully confirmed the formation of helium nuclei as a bound state. The key was a systematic change of the spatial size of the lattice over a sufficiently wide range that allowed a reliable extrapolation to the infinite volume limit. After our finding of the helium nuclei, the NPLQCD Collaboration reported evidence of the H dibaryon bound state in $N_f = 2 + 1$ QCD at $m_\pi = 0.39$ GeV investigating the volume dependence of the energy shift from twice of the Λ baryon mass [2,3]. This was followed by the HALQCD Collaboration which also presented evidence of the H dibaryon, but in degenerate $N_f = 3$ QCD at $m_\pi = 0.67$–1.02 GeV based on analysis with the effective potential measured by the two-baryon wave function [4].

The situation is markedly different for deuteron. This is the simplest nucleus composed of two nucleons in the spin triplet channel, and yet evidence based on lattice QCD for a bound state has never been reported. It is already quite some time ago that a first analysis of the two-nucleon system was made in quenched QCD [5,6]. Much more recently, studies were made with a partially quenched mixed action [7] and $N_f = 2 + 1$ anisotropic Wilson action [2]. Extraction of the potential between two nucleons has been investigated in quenched QCD [8–10]. All these studies, however, tried to calculate the two-nucleon scattering lengths assuming, based primarily on model considerations with nuclear potentials, that the deuteron becomes unbound for the heavy quark mass, corresponding to $m_\pi \gtrsim 0.3$ GeV, employed in their simulations.

It is time to check the validity of this assumption. We need to investigate whether the bound state exists or not in the heavy quark mass region, where studies so far have been carried out, using the arsenal of methods solely within lattice QCD. If there is a bound state, the ground-state energy never yields the scattering length if substituted into Lüscher's finite volume formula [11,12]. In such a case, the scattering length should be obtained from the energy of the first excited state.

We carry out two types of calculations at a heavy quark mass corresponding to $m_\pi = 0.8$ GeV in quenched QCD. The first one is a conventional analysis in which we investigate the volume dependence of the energy shift for the ground state. Different volume dependence is expected for scattering and bound states. In the second one we investigate the energy level of the first excited state employing

the diagonalization method [13] to separate the first excited state from the ground state near the threshold of $2m_N$. If we find the ground state slightly below the threshold and the first excited state slightly above it, then such a configuration of the two lowest levels is consistent with the ground state being a bound state and the first excited state a scattering state with almost zero relative momentum. This method was previously used in a scalar QED simulation to distinguish a system with or without a bound state [14].

Hereafter we call the analyses employed in the first and second calculations the single-state and two-state analyses, respectively. We also refer to the configuration sets used in the two calculations as the first and second ensembles. We should note that the $^3S_1$-$^3D_1$ mixing is neglected in this paper, since we restrict ourselves to measure states in the small relative momentum region.

This paper is organized as follows. Section II presents the results of the single-state analysis in the first calculation together with the simulation details. In Sec. III we explain the operators employed in the diagonalization method and examine the results obtained by the two-state analysis. Conclusions and discussions are summarized in Sec. IV.

II. SINGLE-STATE ANALYSIS

Let us first present the results of the single-state analysis for the $^3S_1$ and $^1S_0$ channels.

A. Simulation details

The first ensemble is exactly the same as in the previous work of Ref. [1]. We explain the parameters once again for clarity.

We generate quenched configurations with the Iwasaki gauge action [15] at $\beta = 2.416$ whose lattice spacing is $a = 0.128$ fm, corresponding to $a^{-1} = 1.541$ GeV, determined with $r_0 = 0.49$ fm as an input [16]. We employ the hybrid Monte Carlo (HMC) algorithm with the Omelyan-Mryglod-Folk integrator [17,18]. The step size is chosen to yield a reasonable acceptance rate presented in Table I. We take three lattice sizes, $L^3 \times T = 24^3 \times 64$, $48^3 \times 48$, and $96^3 \times 48$, to investigate the spatial volume dependence of the energy difference between the two-nucleon ground state and twice the nucleon mass. The physical spatial extents are 3.1, 6.1, and 12.3 fm, respectively.

TABLE I. Number of configurations (N_{conf}), number of measurements on each configuration (N_{meas}), acceptance rate in the HMC algorithm, pion mass (m_π), and nucleon mass (m_N) for the first ensembles.

L	N_{conf}	N_{meas}	Accept ance(%)	m_π (GeV)	m_N (GeV)
24	2500	2	93	0.8000(3)	1.619(2)
48	400	12	93	0.7999(4)	1.617(2)
96	200	12	68	0.8002(3)	1.617(2)

We use the tadpole improved Wilson action with $c_{\mathrm{SW}} = 1.378$ [16]. Since it becomes harder to obtain a reasonable signal-to-noise ratio at lighter quark masses for the multinucleon system, we employ a heavy quark mass at $\kappa = 0.134\,82$ which gives $m_\pi = 0.8$ GeV for the pion mass and $m_N = 1.6$ GeV for the nucleon mass. Statistics is increased by repeating the measurement of the correlation functions with the source points in different time slices on each configuration. The number of configurations and measurements on each configuration are listed in Table I. We separate successive measurements by 100 trajectories with $\tau = 1$ for the trajectory length. The errors are estimated by jackknife analysis choosing 200 trajectories for the bin size.

The quark propagators are solved with the periodic boundary condition in all the spatial and temporal directions using the exponentially smeared source

$$q'(\vec{x}, t) = \sum_{\vec{y}} A e^{-B|\vec{x}-\vec{y}|} q(\vec{y}, t) \tag{1}$$

after the Coulomb gauge fixing. On each volume we employ two sets of smearing parameters: $(A, B) = (0.5, 0.5)$, $(0.5, 0.1)$ for $L = 24$ and $(0.5, 0.5)$, $(1.0, 0.4)$ for $L = 48$ and 96. The onset of the ground state can be confirmed by consistency of effective masses with different sources as shown later. Hereafter the nucleon operators using the first and the second smearing parameter sets are referred to as $\mathcal{O}_1$ and $\mathcal{O}_2$, respectively.

The interpolating operator for the proton is defined as

$$p_\alpha = \varepsilon_{abc}([u_a]^t C\gamma_5 d_b) u_c^\alpha, \tag{2}$$

where $C = \gamma_4\gamma_2$ and α and a, b, c are the Dirac index and the color indices, respectively. The neutron operator n_α is obtained by replacing u_c^α by d_c^α in the proton operator. To save the computational cost we use the nonrelativistic quark operator, in which the Dirac index is restricted to the upper two components.

The two-nucleon operators for the $^3S_1$ and $^1S_0$ channels are given by

$$NN_{^3S_1}(t) = \frac{1}{\sqrt{2}}[p_+(t)n_+(t) - n_+(t)p_+(t)], \tag{3}$$

$$NN_{^1S_0}(t) = \frac{1}{\sqrt{2}}[p_+(t)p_-(t) - p_-(t)p_+(t)]. \tag{4}$$

For the source operator we insert the *smeared* quark fields of Eq. (1) for each nucleon operator located at the same spatial point $\vec{x}$. Each nucleon in the sink operator, on the other hand, is composed of the *point* quark fields, and projected to have zero spatial momentum. We call this type of sink operator the *point sink* operator. In the spin triplet channel the operators for other two spin components are constructed in a similar way. We increase the statistics by averaging over the three spin components.

B. Numerical results

Let us first present the effective mass of the nucleon on the $(6.1\ \mathrm{fm})^3$ box in Fig. 1. We observe that the signals with the $\mathcal{O}_{1,2}$ source operators are clean and the plateaus show reasonable consistency with each other. The exponential fit results with 1 standard deviation errors are denoted by the solid lines. They also show the consistency between the results from the two-nucleon correlation functions.

Figure 2 shows the effective energy plots for the two-nucleon correlation functions with the $\mathcal{O}_{1,2}$ operators in the $^3S_1$ channel on the same volume as in the above. We find clear signals up to $t \approx 12$, beyond which statistical fluctuation dominates. The effective masses with the different sources show a reasonable agreement in the plateau region.

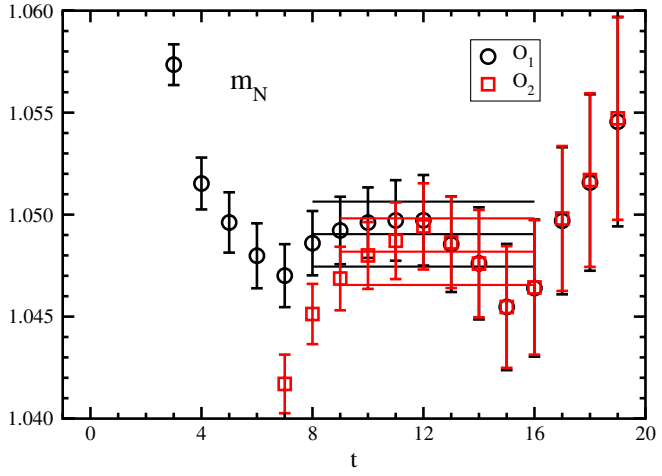

FIG. 1 (color online). Effective mass of nucleon with the $\mathcal{O}_1$ (circle) and $\mathcal{O}_2$ (square) sources on the $(6.1\ \mathrm{fm})^3$ box in lattice units. Fit results with 1 standard deviation error band are expressed by solid lines.

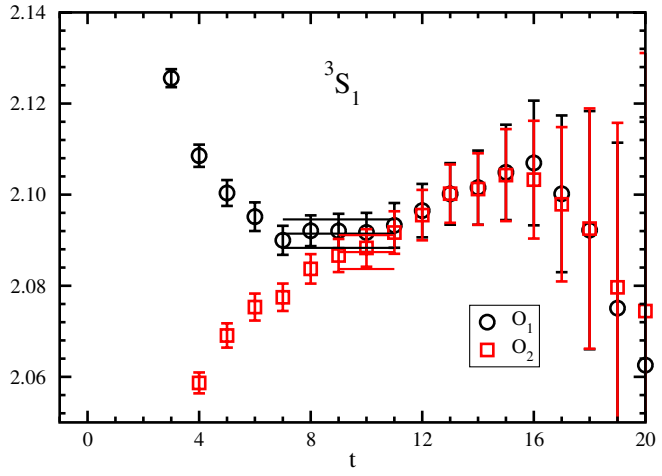

FIG. 2 (color online). Effective energy for the $^3S_1$ channel with the $\mathcal{O}_1$ (circle) and $\mathcal{O}_2$ (square) sources on the $(6.1\ \mathrm{fm})^3$ box in lattice units. Fit results with 1 standard deviation error band are expressed by solid lines.

The result of exponential fit over the plateau region is presented by the solid lines for each operator in the figure. Similar behavior of the effective energy is observed in the $^1S_0$ channel as shown in Fig. 3.

In order to determine the energy shift $\Delta E_L = E_{NN} - 2E_N$ precisely in each volume, we define the ratio of the two-nucleon correlation function divided by the nucleon correlation function squared,

$$R(t) = \frac{G_{NN}(t)}{(G_N(t))^2}, \tag{5}$$

where the same source operator is chosen for $G_{\mathrm{NN}}(t)$ and $G_N(t)$. The effective energy shift is extracted as

$$\Delta E_L^{\mathrm{eff}} = \ln\left(\frac{R(t)}{R(t+1)}\right). \tag{6}$$

In Fig. 4 we present typical results of time dependence of $\Delta E_L^{\mathrm{eff}}$ for the $\mathcal{O}_{1,2}$ sources in the $^3S_1$ channel, both of

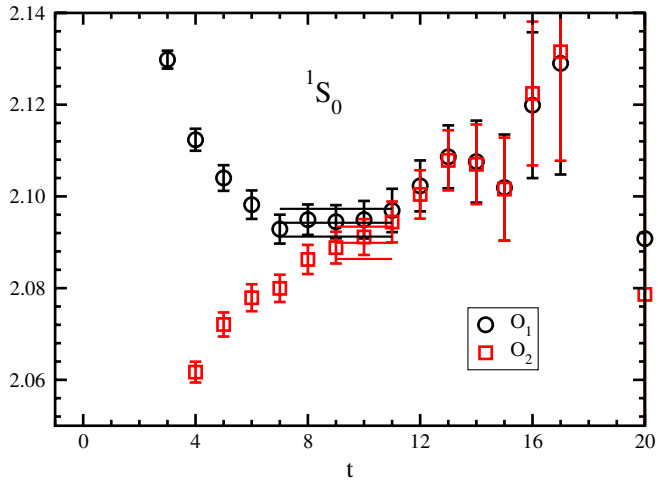

FIG. 3 (color online). Same as Fig. 2 for the $^1S_0$ channel.

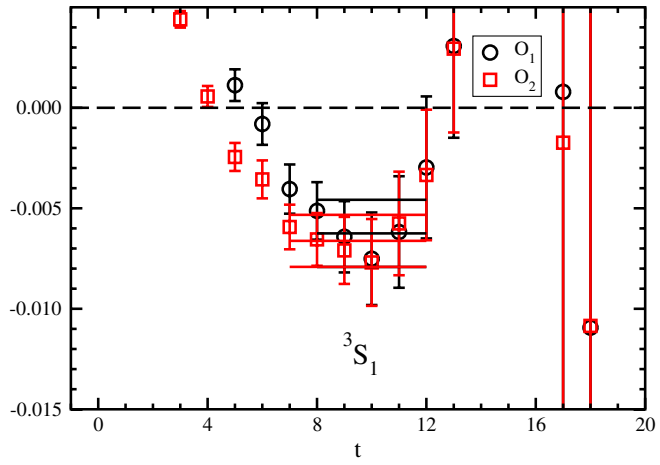

FIG. 4 (color online). Effective energy shift $\Delta E_L^{\mathrm{eff}}$ for the $^3S_1$ channel with the $\mathcal{O}_1$ (circle) and $\mathcal{O}_2$ (square) sources on the $(6.1\ \mathrm{fm})^3$ box in lattice units. Fit results with 1 standard deviation error band are expressed by solid lines.

which show negative values beyond the error bars in the plateau region of $t = 8$–11. Note that this plateau region is reasonably consistent with that for the effective mass of the two-nucleon correlation functions in Fig. 2. The signals of $\Delta E_L^{\rm eff}$ are lost beyond $t \approx 12$ because of the large fluctuations in the two-nucleon correlation functions. We determine ΔE_L by an exponential fit of the ratio in the plateau region, $t = 8$–12 for $\mathcal{O}_1$ and $t = 7$–12 for $\mathcal{O}_2$, respectively. The systematic error of the fit is estimated from the difference of the central values of the fit results with the minimum or maximum time slice changed by ± 1. We obtain a similar quality for the signal for different boxes of $(3.1\ \text{fm})^3$ and $(12.3\ \text{fm})^3$ as shown in Figs. 5 and 6, respectively.

The result for the $^1S_0$ channel on the $(6.1\ \text{fm})^3$ box is shown in Fig. 7. We find that the effective energy shift $\Delta E_L^{\rm eff}$ is negative beyond the error bars, though its absolute value is smaller than the $^3S_1$ case. The energy shift ΔE_L is determined in the same way as for the $^3S_1$ channel.

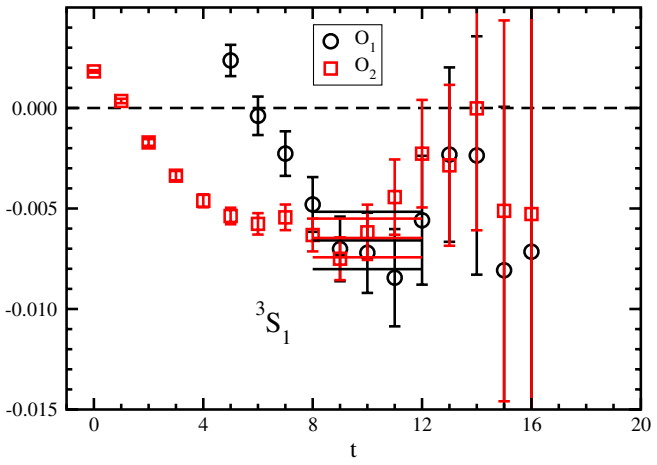

FIG. 5 (color online). Same as Fig. 4 on the $(3.1\ \text{fm})^3$ box.

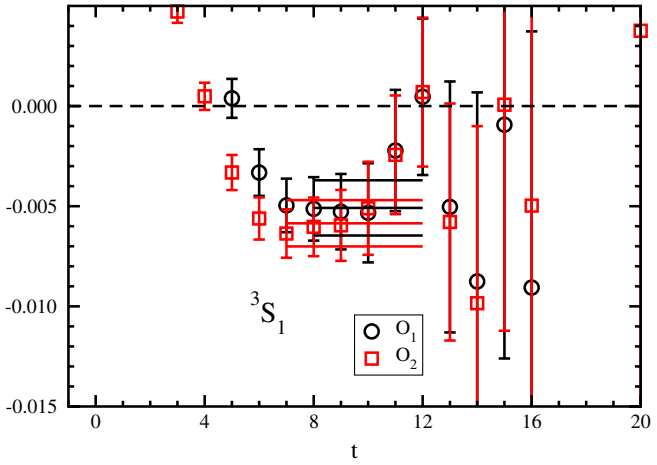

FIG. 6 (color online). Same as Fig. 4 on the $(12.3\ \text{fm})^3$ box.

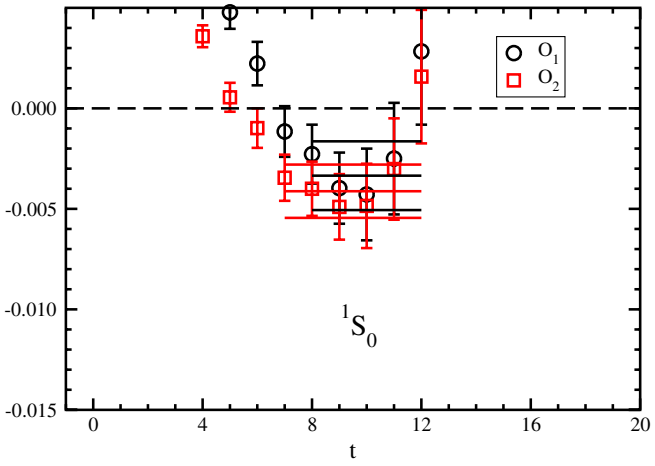

FIG. 7 (color online). Same as Fig. 4 for the $^1S_0$ channel.

The volume dependence of the energy shift ΔE_L for the $^3S_1$ channel is plotted as a function of $1/L^3$ in Fig. 8. Table II summarizes the numerical values of ΔE_L on three spatial volumes, where the statistical and systematic errors are presented in the first and second parentheses, respectively. The results for the $\mathcal{O}_{1,2}$ sources are consistent within the error bars. Little volume dependence for ΔE_L indicates a bound state, rather than the $1/L^3$ dependence expected for a scattering state, for the ground state in the $^3S_1$ channel.

The binding energy in the infinite spatial volume limit in Table II is extracted by a simultaneous fit of the data for the $\mathcal{O}_{1,2}$ sources employing the fit function including a finite volume effect for the two-particle bound state [14,19],

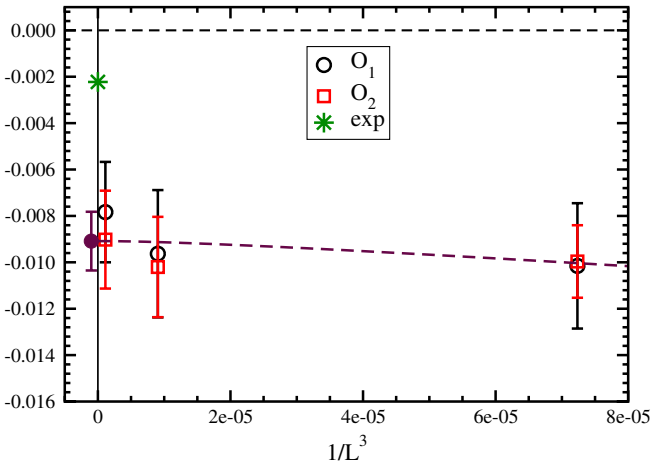

FIG. 8 (color online). Spatial volume dependence of $\Delta E_L = E_{NN} - 2m_N$ in GeV units for the $^3S_1$ channel with the $\mathcal{O}_1$ (circle) and $\mathcal{O}_2$ (square) sources. Statistical and systematic errors are added in quadrature. Extrapolated results to the infinite spatial volume limit (filled circle) and experimental values (star) are also presented.

TABLE II. Energy shift $-\Delta E_L$ in MeV units for $^3S_1$ and $^1S_0$ channels on each spatial volume with the first ensembles. Extrapolated results to the infinite spatial volume limit are also presented. The first and second errors are statistical and systematic, respectively.

	$^3S_1$		$^1S_0$	
L	$\mathcal{O}_1$	$\mathcal{O}_2$	$\mathcal{O}_1$	$\mathcal{O}_2$
24	10.2(2.2)(1.6)	10.0(1.5)(0.5)	6.1(2.3)(2.2)	8.4(1.5)(0.5)
48	9.6(2.6)(0.9)	10.2(2.0)(0.8)	5.2(2.6)(0.8)	6.4(2.0)(0.8)
96	7.8(2.1)(0.4)	9.0(2.0)(0.5)	4.6(2.0)(1.1)	6.0(1.9)(0.5)
∞	9.1(1.1)(0.5)		5.5(1.1)(1.0)	

$$\Delta E_L = -\frac{\gamma^2}{m_N}\left\{1 + \frac{C_\gamma}{\gamma L}\sum_{\vec{n}}{}' \frac{\exp(-\gamma L\sqrt{\vec{n}^2})}{\sqrt{\vec{n}^2}}\right\}, \quad (7)$$

where γ and C_γ are free parameters, $\vec{n}$ is a three-dimensional integer vector, and $\sum'_{\vec{n}}$ denotes the summation without $|\vec{n}| = 0$. The binding energy, $-\Delta E_\infty$, is determined from γ,

$$-\Delta E_\infty = -\frac{\gamma^2}{m_N}, \quad (8)$$

where we assume

$$2\sqrt{m_N^2 - \gamma^2} - 2m_N \approx -\frac{\gamma^2}{m_N}. \quad (9)$$

The systematic error is estimated from the difference of the central values of the fit results choosing different fit ranges in the determination of ΔE_L, and also using a constant fit as an alternative fit form. Adding the statistical and systematic errors by quadrature, we obtain $-\Delta E_\infty = 9.1(1.3)$ MeV for the binding energy.

We conclude that the ground state in the $^3S_1$ channel is a bound state. The provisos, of course, are that pion mass is quite heavy and that quark vacuum polarizations are left out. Whether these are the reasons why the binding energy is about 4 times larger than the experimental value, 2.22 MeV, is an interesting issue for future study with lighter pion mass in full QCD.

Figure 9 plots the volume dependence of the energy shift ΔE_L for the $^1S_0$ channel, whose numerical values are summarized in Table II. Employing the same analysis as in the $^3S_1$ channel, we find that $-\Delta E_\infty = 5.5(1.5)$ MeV in the infinite volume limit, which is 3.7σ away from zero. This tells us that the ground state in the $^1S_0$ channel is also bound at $m_\pi = 0.8$ MeV. Since the existence of the bound state in this channel is not expected at the physical quark mass, it might be a consequence of much heavier quark mass used in our calculation. Although there are several model calculations varying the up- and down-quark masses, they are restricted around the physical values [20–23]. It is an intriguing subject to check if the bound state in the $^1S_0$ channel disappears at lighter quark masses. This is beyond the scope of this paper, however.

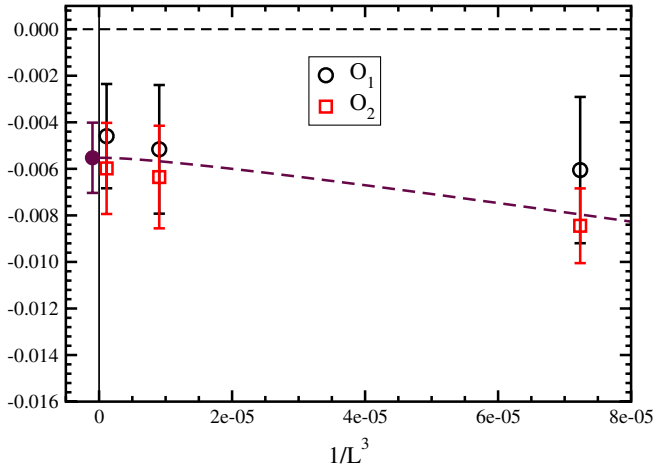

FIG. 9 (color online). Same as Fig. 8 for the $^1S_0$ channel.

In the nuclear potential approach [24], the phase shift for the $^1S_0$ channel was reported in $N_f = 2 + 1$ QCD at a similar quark mass of $m_\pi \sim 0.7$ GeV, which does not show a signal for a bound state. Examination on systematic errors such as the spatial volume dependence and excited state contaminations is needed to see if the two methods lead to contradictory conclusions.

III. TWO-STATE ANALYSIS

In this section we present the results of analysis with the diagonalization method [13]. The focus of the analysis is the characteristic feature, well known from quantum mechanics, that the existence of a bound state implies a scattering state just above the two-particle threshold, and hence a negative scattering length. Our investigation is carried out with the diagonalization of 2×2 correlation function matrix.

A. Simulation details

We work with two spatial extents, 4.1 fm and 6.1 fm. The corresponding lattice sizes are $L^3 \times T = 32^3 \times 48$ and $48^3 \times 48$, respectively. The latter is the same size as in the first ensemble, but we regenerate independent configurations employing the same algorithm. Most of the simulation parameters, including the gauge and fermion actions, lattice spacing, and quark mass, are identical to those explained in Sec. II. However, the number of configurations and the separation of trajectories between each measurement, and the number of measurements on each configuration are different. These numbers are tabulated in Table III. The errors are estimated by the jackknife analysis choosing 400 and 200 trajectories for the bin size on the $(4.1\ \text{fm})^3$ and $(6.1\ \text{fm})^3$ boxes, respectively. These bin sizes are sufficiently large to remove the autocorrelation. We use the same operators for the nucleons and two-nucleons as in Eqs. (2)–(4), choosing the nonrelativistic components.

TABLE III. Number of configurations ($N_{\rm conf}$), separation of trajectories between each measurement ($N_{\rm sep}$), number of measurements with $\mathcal{O}_1$ source on each configuration ($N_{\rm meas}$), number of $Z(3)$ random number for O_r source on each configuration ($N_{\rm rand}$), spatial interval between smeared quark fields for $\mathcal{O}_r$ source ($N_{\rm mod}$), acceptance rate in the HMC algorithm, pion mass (m_π), and nucleon mass (m_N) for the second ensembles.

L	$N_{\rm conf}$	$N_{\rm sep}$	$N_{\rm meas}$	$N_{\rm rand}$	$N_{\rm mod}$	Acceptance (%)	m_π (GeV)	m_N (GeV)
32	300	400	192	40	16	87	0.7998(2)	1.6162(9)
48	300	200	144	32	12	93	0.8001(1)	1.6176(4)

The diagonalization method for the 2×2 matrix requires two operators each at source and sink time slice, which are explained in the following subsections.

1. Source operators

We use the two-nucleon operator composed of the $\mathcal{O}_1$ nucleon operator explained in Sec. II as one of the source operators for diagonalization; from the single-state analysis, we expect that it has good overlap with the ground state of the two-nucleon system. To reduce the statistical error as much as possible we carry out more than 100 measurements on each configuration by changing the center of the smearing source in the spatial and temporal directions.

The diagonalization procedure requires another operator which reasonably overlaps to the first excited state. If we envisage this to be a scattering state of the two nucleons with almost zero relative momentum, then a possible candidate is an operator consisting of two nucleons each projected to zero spatial momentum. Constructing such an operator at the source time slice can be done using $Z(3)$ noises for the quark fields. It is empirically known, however, that statistical noise overwhelms signal in the (multi)nucleon correlation function if the noise is spread over the entire spatial volume.

The large fluctuation can be reduced by restricting noise to a subset of lattice sites at a fixed separation of $N_{\rm mod}$ in each spatial dimension at the source time slice. This source operator, which we shall call the $\mathcal{O}_r$ source, is defined by

$$\mathcal{O}_r(t) = \frac{1}{N_{\rm rand}} \sum_{j=1}^{N_{\rm rand}} \Big[\sum_{\vec{x} \in V'} \xi_j(\vec{x}) q'(\vec{x}, t) \Big]^3, \qquad (10)$$

where $N_{\rm rand}$ is the number of the noise, and the color and Dirac indices of the quark field are omitted for simplicity. We use the smeared quark fields $q'(\vec{x}, t)$ of Eq. (1) after Coulomb gauge fixing, whose parameters are the same as in the $\mathcal{O}_1$ source $(A, B) = (0.5, 0.5)$ to obtain faster plateau of the nucleon state. The smeared quark field is located at

$$V' = \{\vec{x} = \vec{x}_0 + \vec{n} N_{\rm mod}, (\vec{x})_i < L\}, \qquad (11)$$

with $\vec{x}_0$ being a reference position, $(\vec{x}_0)_i < N_{\rm mod}$, and $\vec{n}$ being three-dimensional integer vector. The complex $Z(3)$ random number $\xi_j(\vec{x})$ satisfies $(\xi_j(\vec{x}))^3 = 1$ and has the property

$$\lim_{N_{\rm rand} \to \infty} \frac{1}{N_{\rm rand}} \sum_{j=1}^{N_{\rm rand}} \xi_j(\vec{x}) \xi_j(\vec{y}) \xi_j(\vec{z}) = \delta_{\vec{x},\vec{y}} \delta_{\vec{x},\vec{z}}. \qquad (12)$$

The parameters $N_{\rm mod}$ and $N_{\rm rand}$ for each calculation are summarized in Table III.

2. Sink operators

We also need two operators on the sink side to carry out diagonalization. Our idea is to employ the solution of the Helmholtz equation in three dimensions for the smearing function of the two-nucleon sink operator,

$$W_{q^2}(\vec{r}) = C_{q^2} \sum_{\vec{n}} \frac{e^{i(2\pi/L)\vec{n}\cdot\vec{r}}}{\vec{n}^2 - q^2}, \qquad (13)$$

where q^2 is a parameter, $\vec{r}$ is the relative coordinate between two nucleons, and $\vec{n}$ is a three-dimensional integer vector. The overall factor C_{q^2} is determined from the normalization condition $|W_{q^2}(\vec{r}_{\rm max})| = 1$. A similar calculation using the solution of the Helmholtz equation was previously reported in Ref. [25].

In the region of $|\vec{r}|$ closer to the origin, the smearing function should be modified from the free form to take into account the two-particle interaction. One way is to calculate the two-particle wave function, as has been done for the two-pion system [26,27] and the two-nucleon systems [8–10], and use it as input. We take a simpler alternative of modifying the smearing function by hand such that it behaves as a smooth constant function around the origin rather than a sharp increase or decrease which occurs for the free form.

The value of q^2 is related to the relative momentum of the two-nucleon state as $p^2 = (2\pi/L)^2 \cdot q^2$, where q^2 is not an integer in general due to the finite volume effect of the two-particle interaction [11,12]. Since we need two smearing functions, we take a pair of values of q^2, one around zero momentum $q^2 \approx 0$ and the other around unit of momentum $q^2 \approx 1$ being the simplest choices, and make trial runs to find the optimum values of q^2. We choose the value of q^2 such that the measured energy of the ground state is statistically consistent with the one obtained in the single-state analysis, and the onset of the plateau of the ground state becomes faster than the one in the single-state analysis. Because of our criteria of the choice of q^2, this analysis does not provide an independent check for the

ground-state energy against the single-state analysis. After several trial calculations, we choose $q^2 = 0.184$ and 1.3 for the $(4.1\ \mathrm{fm})^3$ box, and $q^2 = 0.1$ and 1.1 for the $(6.1\ \mathrm{fm})^3$ box. Our smearing functions for both volumes are plotted in Figs. 10 and 11.

We note that we do not use a negative q^2 determined from the bound state which corresponds to an exponentially damped smearing function. In the two-nucleon correlation function for the $\mathcal{O}_1$ source and such a sink operator, we find that higher excited state contributions are not suppressed. Hence such an operator is not suitable for the 2×2 diagonalization of the ground and first excited states we attempt to carry out.

Let us finally note that we also employ the point sink operator to carry out the single-state analysis on the second ensemble for a consistency check with the results from the first ensemble.

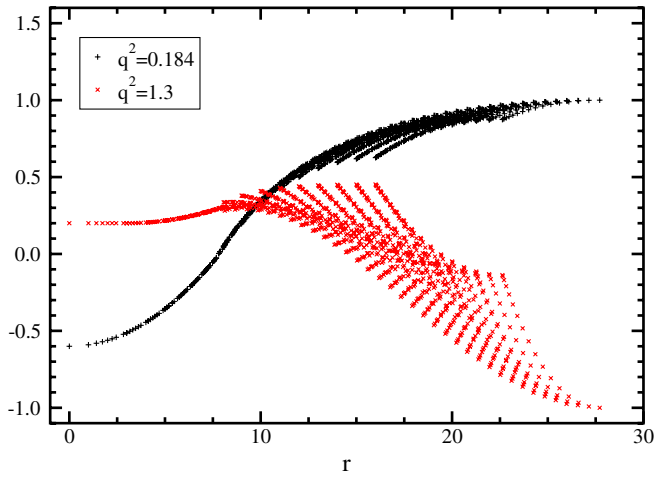

FIG. 10 (color online). Smearing functions of the sink operator on the $(4.1\ \mathrm{fm})^3$ box for two-state analysis.

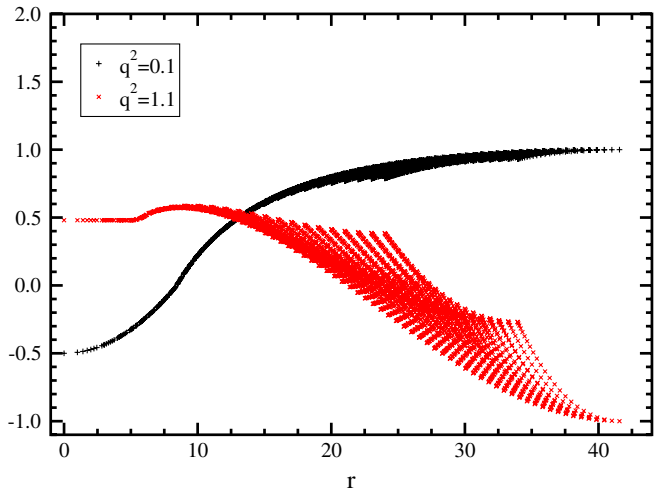

FIG. 11 (color online). Same as Fig. 10 on the $(6.1\ \mathrm{fm})^3$ box.

B. Results for $(6.1\ \mathrm{fm})^3$ box

We first show the results for the $^3S_1$ channel on the $(6.1\ \mathrm{fm})^3$ box. Let us begin with data for the $\mathcal{O}_1$ source. Figure 12 shows the effective energies in the $^3S_1$ channel for the two smearing function sinks, $W_{0.1}$ and $W_{1.1}$, and the point sink P. The effective energy for the $W_{0.1}$ smearing function diverges around $t = 8$, and rises up from below after $t = 12$ due to the sign flip of the correlation function. Thus at least two states contribute to the correlation function overlapping to the operator with different signs. On the other hand, the result for $W_{1.1}$ is close to that for the point sink P. Figure 13 is an expanded view on this point.

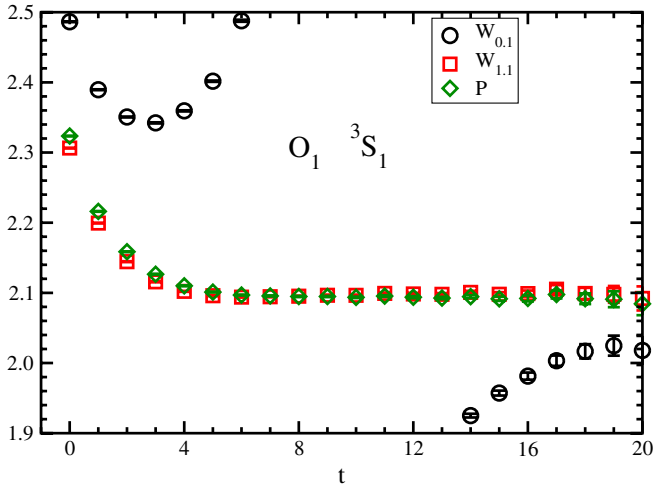

FIG. 12 (color online). Effective energy for the $^3S_1$ channel with the $\mathcal{O}_1$ source on the $(6.1\ \mathrm{fm})^3$ box. Results are given in lattice units with smearing functions $W_{0.1}$ (circle) and $W_{1.1}$ (square), and point sink operator (diamond).

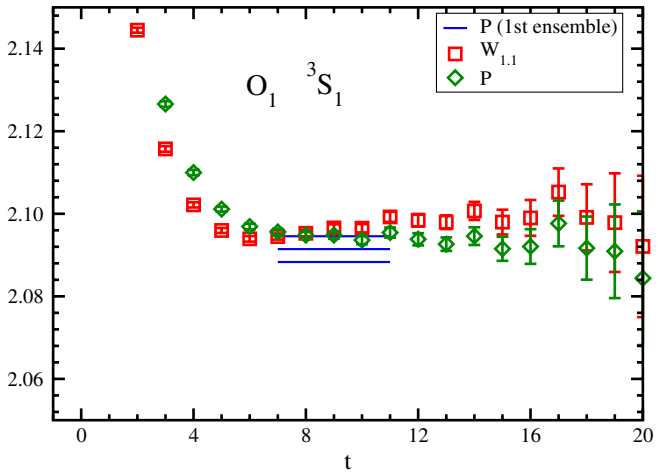

FIG. 13 (color online). Same as Fig. 12, but scale in vertical axis is enlarged. Solid lines denote fit result for ground-state energy with 1 standard deviation error band in single-state analysis choosing the $\mathcal{O}_1$ source.

Let us now look at effective energies for the $\mathcal{O}_r$ source in Fig. 14. In this case the $W_{0.1}$ result is close to the point sink result, whereas the $W_{1.1}$ result is lower.

We diagonalize the following matrix at each t:

$$M(t, t_0) = C(t_0)^{-1}C(t), \tag{14}$$

where t_0 is a reference time and the 2×2 components of the correlation function matrix $C(t)$ are given by

$$C_{ij}(t) = G_{NN}^{i;j}(t), \tag{15}$$

with $G_{NN}^{i;j}(t)$ being the two-nucleon correlation function using the i ($i = \mathcal{O}_1$, $\mathcal{O}_r$) source operator and the j ($j = W_{0.1}, W_{1.1}$) smearing function for the sink operator. With a choice of $t_0 = 6$ we determine the two eigenvalues $\lambda_\alpha(t)$ ($\alpha = 0, 1$) of $M(t, t_0)$ at each t and extract the energy of each eigenstate α through $\lambda_\alpha(t) = \exp(-\bar{E}_{L,\alpha}(t - t_0))$.

The effective energies of the eigenstates obtained from the diagonalization are plotted in Fig. 15. The energies for the two states are clearly separated in the plateau region. The ground state result is reasonably consistent with the result of the single-state analysis with the $\mathcal{O}_1$ source obtained on the first ensemble, which is expressed by the three solid lines in the figure. The first excited state is clearly higher than the ground state, but it is much lower than the free case with the lowest relative momentum, whose energy is given by $2\sqrt{m_N^2 + (2\pi/L)^2}$ denoted by the single solid line in the figure. We note that our present analysis ignores possible systematic errors arising from contaminations from second and higher excited states. Examining this issue with a larger size correlation function is left for future studies.

In order to determine the energy shift as in Sec. II, we define the ratio of the eigenvalue obtained from the diagonalization to the nucleon correlation function squared,

$$\bar{R}_\alpha(t) = \frac{\lambda_\alpha(t)}{(G_N(t))^2}. \tag{16}$$

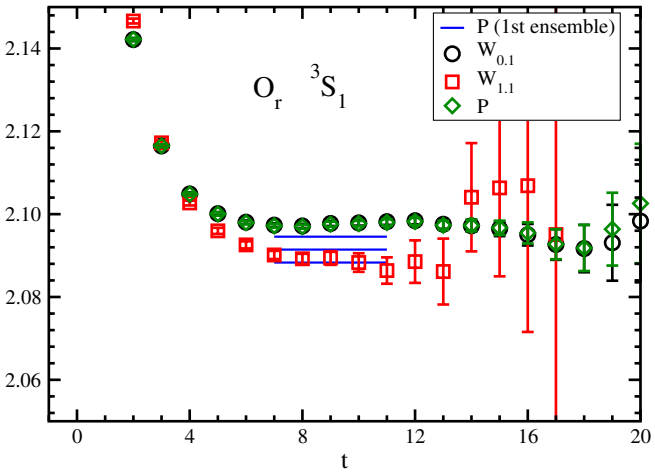

FIG. 14 (color online). Same as Fig. 13 with the $\mathcal{O}_r$ source.

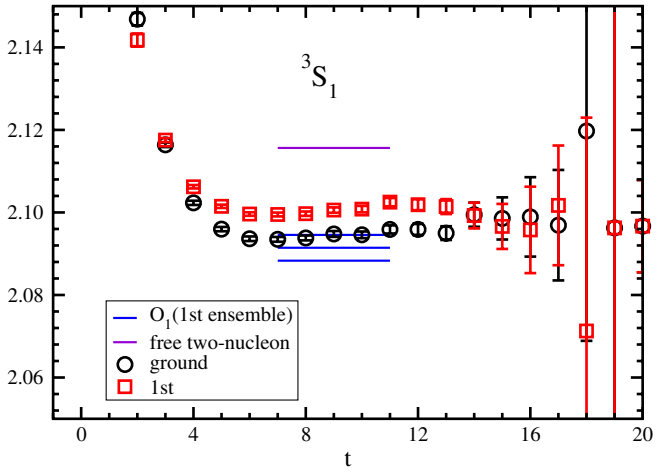

FIG. 15 (color online). Effective energy of two-nucleon ground (circle) and first excited (square) states obtained by the diagonalization method for the $^3S_1$ channel in lattice units. Fit result of single-state analysis with the $\mathcal{O}_1$ source on the first ensemble with 1 standard deviation error band is expressed by three solid lines. Expected energy level of free two-nucleon state with lowest relative momentum is denoted by single solid line.

We also define the effective energy shift of the ratio $\bar{R}_\alpha$ as

$$\Delta\bar{E}_{L,\alpha}^{\text{eff}} = \ln\left(\frac{\bar{R}_\alpha(t)}{\bar{R}_\alpha(t+1)}\right). \tag{17}$$

1. Ground state in the $^3S_1$ channel

Figure 16 shows a compilation of all data for the ground state both from the diagonalization analysis as well as from

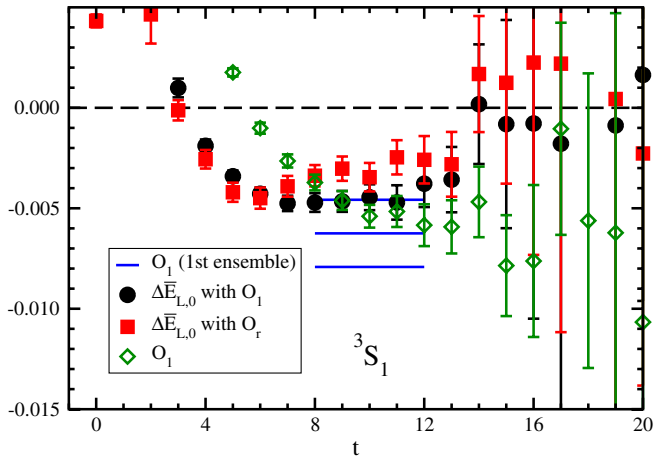

FIG. 16 (color online). Effective energy shifts $\Delta\bar{E}_{L,0}^{\text{eff}}$ for the $^3S_1$ channel on the $(6.1\text{ fm})^3$ box in lattice units. Nucleon correlators with the $\mathcal{O}_1$ (circle) and $\mathcal{O}_r$ (square) sources are employed in the denominator of Eq. (16). Result of single-state analysis with the $\mathcal{O}_1$ source ΔE_L^{eff} is also plotted by open diamonds. Fit result of single-state analysis with the $\mathcal{O}_1$ source on the first ensemble with 1 standard deviation error band is given by solid lines.

the single-state analysis. The solid circles represent the effective energy shift of the ground state $\Delta\bar{E}^{\rm eff}_{L,0}$ using the $\mathcal{O}_1$ source in the nucleon propagator in the denominator of Eq. (16). The solid squares are the ones using the $\mathcal{O}_r$ source in the nucleon propagator. The diamonds show the energy shift from single-state analysis using point sink, but based on the second ensemble. Finally the three lines show the estimated ground-state energy shift from the single-state analysis of the $\mathcal{O}_1$ source with the point sink from the first ensemble.

We find it gratifying that the diagonalization results for the ground state exhibit clear plateaus over a significant time range extending from $t = 7$. A somewhat higher value of the plateau if one takes the $\mathcal{O}_r$ source in the nucleon propagator can be traced back to a systematic shift in the nucleon effective mass itself [see Fig. 17], so that the difference should be regarded as a measure of systematic error. The plateaus are also consistent with the result of the single-state analysis from the same ensemble (diamonds), which in turn are also consistent with that from the first ensemble (solid lines).

We determine the central value of the energy shift from the exponential fit of the $\bar{R}_0(t)$ using the nucleon correlation function of the $\mathcal{O}_1$ source with the fit range of $t = 7$–13. The systematic error due to an estimate of the threshold $2m_N$ is made from the difference between the two results with the $\mathcal{O}_1$ and $\mathcal{O}_r$ sources for the nucleon correlators in the denominator of the $\bar{R}_0$. The systematic error associated with the fit range is estimated by changing the maximum or minimum time slice of the fit range by ± 1. Table IV summarizes the numerical values for the energy shift from the diagonalization analysis $\Delta\bar{E}_{L,0}$, and the single-state analysis ΔE_L. The statistical and systematic errors are presented in the first and second parentheses,

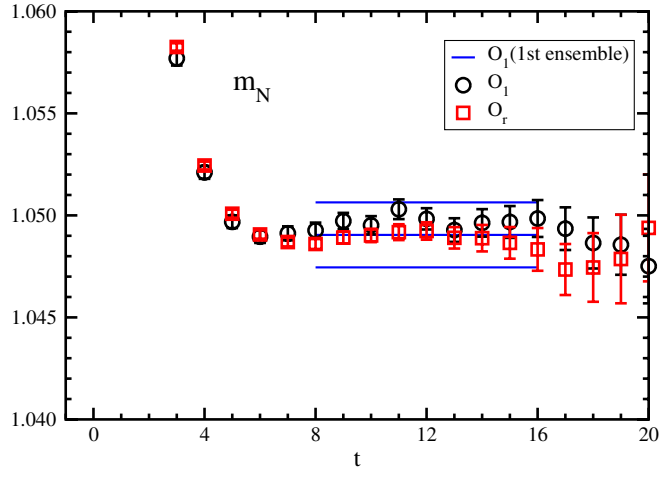

FIG. 17 (color online). Nucleon effective mass on the $(6.1\ \text{fm})^3$ box for the second ensemble with the $\mathcal{O}_1$ (circle) and $\mathcal{O}_r$ (square) sources in lattice units. Fit result of the $\mathcal{O}_1$ source on the first ensemble with 1 standard deviation error band is expressed by solid lines.

TABLE IV. Energy shifts $-\Delta E_L$ and $-\Delta\bar{E}_{L,0}$ in MeV units for $^3S_1$ and $^1S_0$ channels at $L = 32$ and 48 on the second ensembles. The first and second errors are statistical and systematic, respectively.

	$^3S_1$		$^1S_0$	
L	$-\Delta E_L$	$-\Delta\bar{E}_{L,0}$	$-\Delta E_L$	$-\Delta\bar{E}_{L,0}$
32	7.9(0.6)(0.8)	$6.4(1.3)(^{+0.7}_{-0.1})$	4.7(0.7)(0.6)	$3.0(1.7)(^{+0.7}_{-0.3})$
48	8.5(1.1)(0.3)	$7.1(0.7)(^{+0.1}_{-2.2})$	4.8(1.0)(0.7)	$4.5(0.9)(^{+0.1}_{-2.1})$

respectively. We employ an asymmetric systematic error for $\Delta\bar{E}_{L,0}$ to properly reflect an upward shift for the $\mathcal{O}_r$ source relative to the $\mathcal{O}_1$ source.

2. First excited state in the $^3S_1$ channel

Figure 18 shows the effective energy shift of the first excited state $\Delta\bar{E}^{\rm eff}_{L,1}$. Once again, we find a long plateau for both $\mathcal{O}_1$ and $\mathcal{O}_r$ whose values are mutually consistent. The very important feature is that the plateaus are definitively above the threshold and significantly lower than the value expected from the free two-nucleon state with unit relative momentum as presented by the single solid line in the figure. This is consistent with the ground state being a bound state.

The energy shift $\Delta\bar{E}_{L,1}$ is determined from an exponential fit of the $\bar{R}_1(t)$ using the $\mathcal{O}_1$ source nucleon correlator with the fit range of $t = 7$–13. We use the fit result for the $\mathcal{O}_r$ source nucleon correlator to estimate a systematic error of the energy shift. The numerical value is given in Table V.

3. Analysis of the $^1S_0$ channel

In the $^1S_0$ channel, the behaviors of the two-nucleon correlation functions are similar to those in the $^3S_1$ channel, so that we will present only the results after the

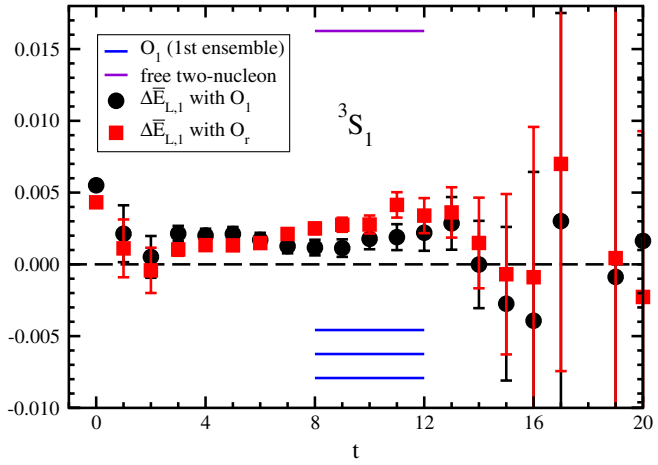

FIG. 18 (color online). Same as Fig. 16 for the first excited state. Expected energy level of free two-nucleon state with lowest relative momentum is denoted by single solid line.

TABLE V. Energy shift of the first excited state $\Delta\bar{E}_{L,1}$ and scattering length a_0 for $^3S_1$ and $^1S_0$ channels at $L = 32$ and 48 after diagonalization in two-state analysis. The first and second errors are statistical and systematic, respectively.

	$^3S_1$		$^1S_0$	
L	$\Delta\bar{E}_{L,1}$ (MeV)	a_0 (fm)	$\Delta\bar{E}_{L,1}$ (MeV)	a_0 (fm)
32	$13.3(1.3)(^{+6.6}_{-1.7})$	$-1.5(0.2)(^{+0.2}_{-1.4})$	$15.8(1.6)(^{+9.6}_{-0.3})$	$-1.8(0.3)(^{+0.4}_{-12.9})$
48	$2.3(0.8)(^{+2.2}_{-0.1})$	$-1.05(24)(^{+0.05}_{-0.65})$	$4.2(0.8)(^{+2.1}_{-0.0})$	$-1.62(24)(^{+0.01}_{-0.75})$

diagonalization. The effective energies of the eigenstates are shown in Fig. 19. The signals are clean and both results show clear plateaus. We observe that the ground-state energy is consistent with the result on the first ensemble of $(6.1\ \text{fm})^3$ box denoted by the three solid lines.

In Figs. 20 and 21 the effective energy shift for the ground and first excited states $\Delta\bar{E}^{\text{eff}}_{L,\alpha}$ are, respectively, shown as well as the result of $\Delta E^{\text{eff}}_{L}$ for the ground state calculated on the second ensemble. We find features similar to those in the $^3S_1$ channel, including long plateaus and

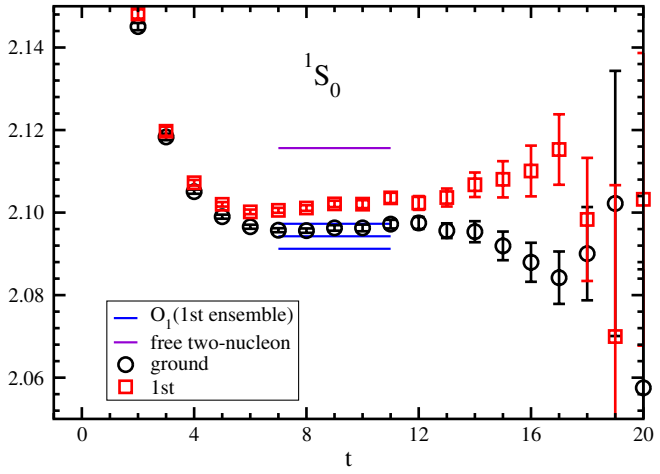

FIG. 19 (color online). Same as Fig. 15 for the $^1S_0$ channel.

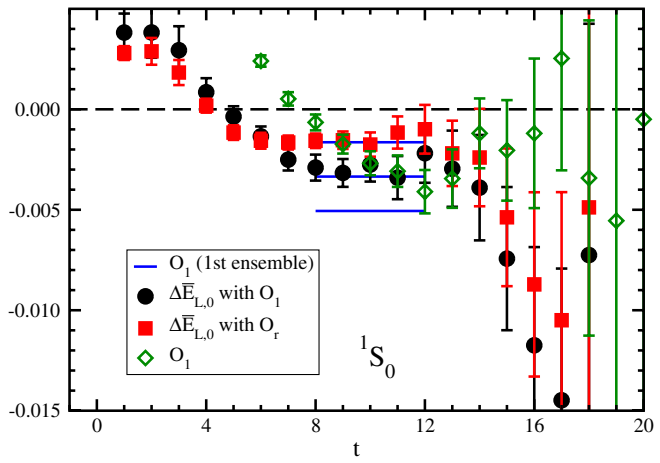

FIG. 20 (color online). Same as Fig. 16 for the $^1S_0$ channel.

systematic biases due to the choice of the source operators. The results for energy shift for the ground and first excited states are summarized in Tables IV and V, respectively, where the errors are estimated as in the $^3S_1$ channel.

We observe that the absolute value of the energy shift of the ground state is almost half of that in the $^3S_1$ channel. This is consistent with the observation in the first calculation. On the other hand, the energy shift of the first excited state shown in Fig. 21 is almost twice larger than that in the $^3S_1$ channel in Fig. 18. This finding is consistent with the property of a system which contains a shallow bound state: The scattering length negatively increases as the binding energy decreases, diverging when the binding energy vanishes.

We confirm then that the two-nucleon system in the $^1S_0$ channel at the heavy quark mass of $m_\pi = 0.8$ GeV has a bound state as in the $^3S_1$ channel.

C. Results for $(4.1\ \text{fm})^3$ box

Scattering states have sensitive dependence on the spatial volume whereas bound states do not change much once the spatial size is sufficiently large to contain them. We repeated the diagonalization analysis on a $(4.1\ \text{fm})^3$ box to examine if such a difference of the two types of states can be confirmed for the ground and first excited states in our case.

The effective energies of the two-nucleon correlation functions with the $\mathcal{O}_1$ and $\mathcal{O}_r$ source operators for the

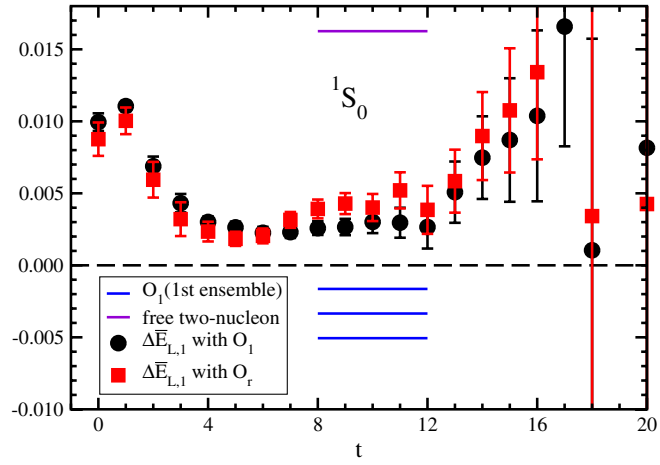

FIG. 21 (color online). Same as Fig. 18 for the $^1S_0$ channel.

$^3S_1$ channel are plotted in Figs. 22 and 23, respectively. The behavior we observe is similar to the case of the $(6.1\ \mathrm{fm})^3$ box except that the effective energy with the smearing function $W_{1.3}$ has a visible slope in the region where the point sink result shows a plateau.

Figure 24 presents the diagonalization results for the two-nucleon effective energy employing $t_0 = 8$ for the reference time in Eq. (14). For the ground state, it is once again gratifying to find a plateau over a sizable range of time, with the value consistent with that from the single-state analysis. However, the effective energy for the first excited state exhibits a visible slope, which was not seen in the $(6.1\ \mathrm{fm})^3$ box case. The positive slope in the first excited state indicates the presence of contaminations from higher excited state in the correlation functions.

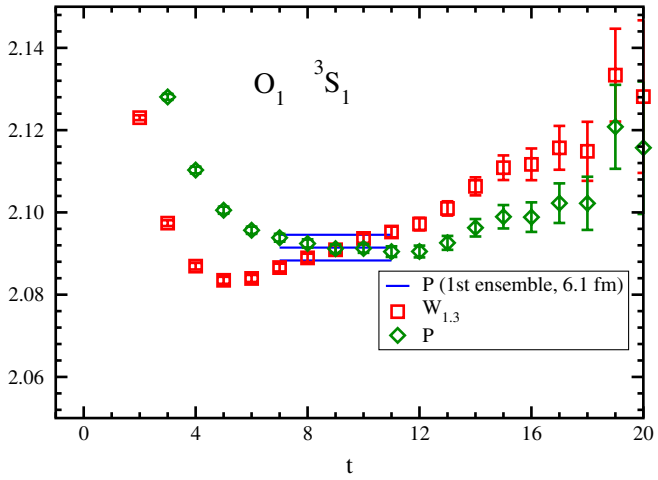

FIG. 22 (color online). Effective energy of the $\mathcal{O}_1$ source on the $(4.1\ \mathrm{fm})^3$ box for the $^3S_1$ channel in lattice units with smearing function $W_{1.3}$ (square) and point sink operator (diamond). Fit result of single-state analysis with the $\mathcal{O}_1$ source on the first ensemble of $(6.1\ \mathrm{fm})^3$ with 1 standard deviation error band is denoted by solid lines.

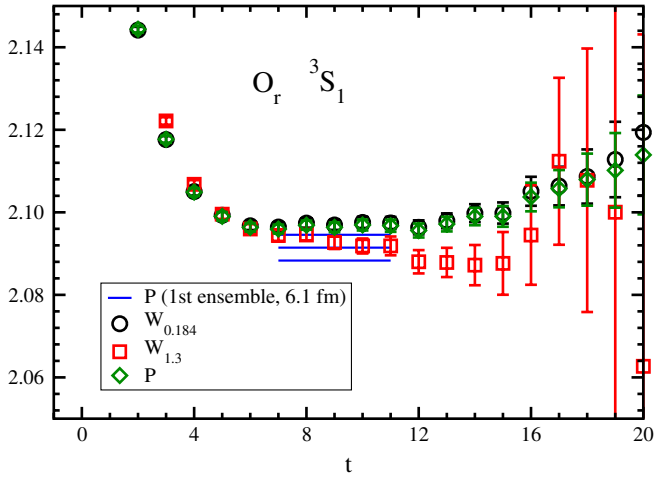

FIG. 23 (color online). Same as Fig. 22 with the $\mathcal{O}_r$ source.

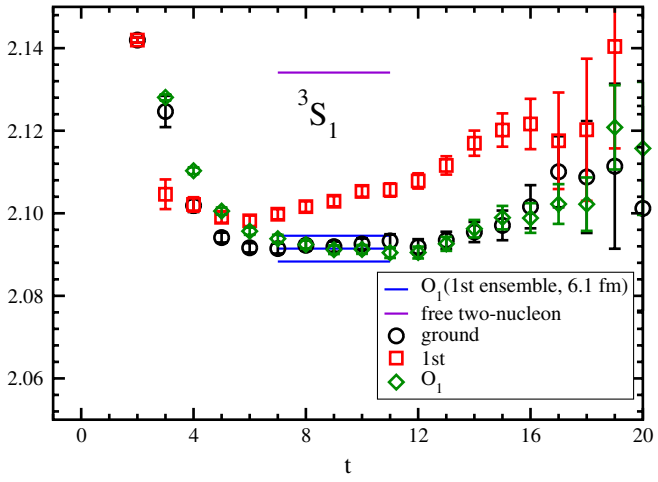

FIG. 24 (color online). Same as Fig. 15 on the $(4.1\ \mathrm{fm})^3$ box. Result of single-state analysis is denoted by diamonds.

While the present results are not as satisfactory as for the $(6.1\ \mathrm{fm})^3$ box case, we find it encouraging that the energy shift relative to the two-nucleon threshold, which is negative for the ground state, is clearly positive for the first excited state and is much lower than the value expected for relative momentum of $2\pi/L$; see Fig. 25. Because of the presence of a positive slope, the estimate of the energy shift suffers from a sizable systematic error from the choice of the fit range. We estimate it by making three fits over the ranges $t = 9$–13, 11–13, or 12–14, and taking the difference from the first one which we use as the central value. For the ground state we use $t = 9$–13 as the central fit range, and shift the minimum and maximum time by ± 1. The systematic error due to the choice of the $\mathcal{O}_1$ or $\mathcal{O}_r$ source is also taken into account. The results are summarized in Tables IV and V for the ground and first excited

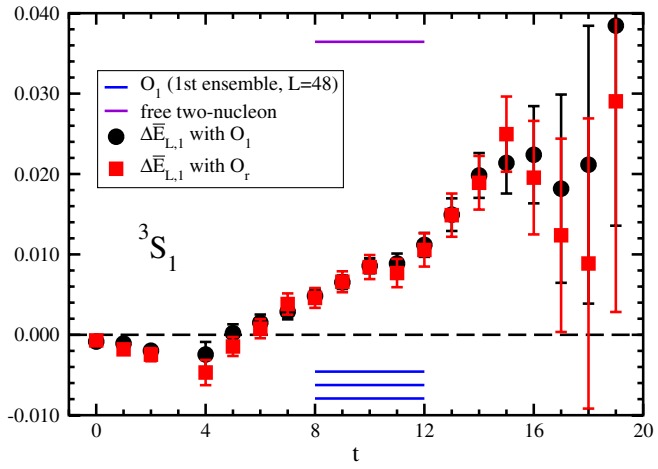

FIG. 25 (color online). Same as Fig. 18 on the $(4.1\ \mathrm{fm})^3$ box.

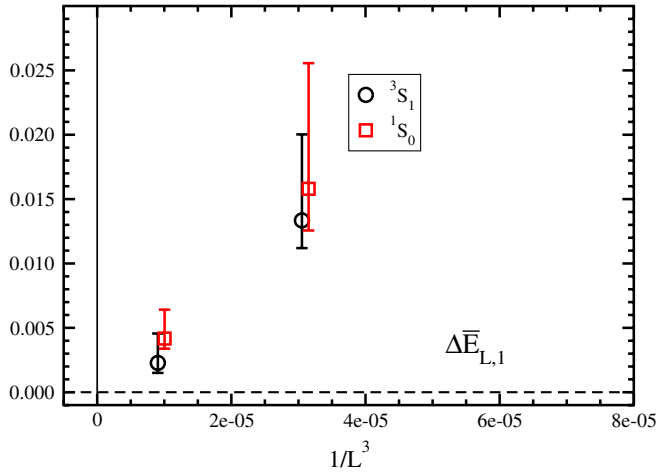

FIG. 26 (color online). Spatial volume dependence of $\Delta\bar{E}_{L,1}$ in GeV units for the first excited states in the $^3S_1$ (circle) and $^1S_0$ (square) channel. The squares are slightly shifted to positive direction in the horizontal axis for clarity. Statistical and systematic errors are added in quadrature.

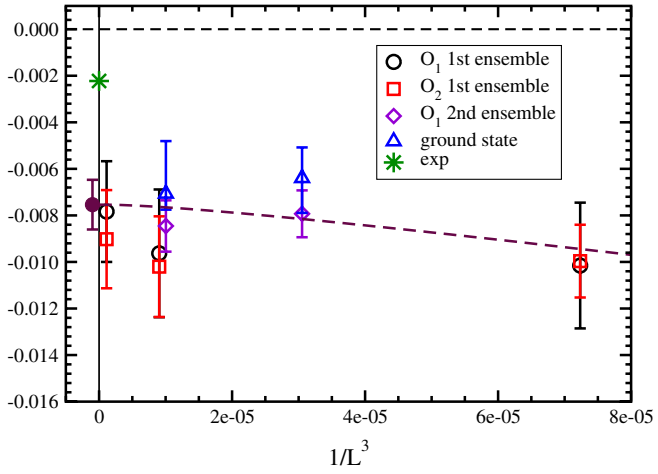

FIG. 27 (color online). Spatial volume dependence of ΔE_L and $\Delta\bar{E}_{L,0}$ in GeV units for the $^3S_1$ channel with a $\mathcal{O}_1$ (circle), $\mathcal{O}_2$ (square) sources on the first ensembles, and a O_1 source on the second ensemble (diamond). Result of $\Delta\bar{E}_{L,0}$ obtained by the diagonalization method is denoted by triangles. The diamond and triangle at $1/L^3 \approx 10^{-5}$ are slightly shifted to positive direction in horizontal axis for clarity. Statistical and systematic errors are added in quadrature. Extrapolated results to the infinite spatial volume limit (filled circle) and experimental values (star) are also presented.

states, respectively, on the $(4.1\ \mathrm{fm})^3$ box for both the $^3S_1$ and $^1S_0$ channels.

In Fig. 26 we plot the energy shift for the first excited state from the two lattice volumes as a function of $1/L^3$. A roughly linear behavior, with a larger shift on the $(4.1\ \mathrm{fm})^3$ box compared to a smaller shift on the $(6.1\ \mathrm{fm})^3$ box, is consistent with this state being a scattering state. We evaluate the scattering lengths using Lüscher's finite volume formula [11,12], and list them in Table V, where we find reasonable consistency between the two volumes. If our finding of a bound state in quenched QCD at heavy quark mass smoothly continues to the physical point, then this is the first calculation which explained a negative scattering length for the deuteron channel.

D. Binding energy from the two calculations

We evaluate the binding energy of the bound state in the $^3S_1$ and $^1S_0$ channels using the combined results obtained from both the first and second calculations. Figures 27 and 28 are the same as Figs. 8 and 9, respectively, but including the results of the second calculations. The new data are reasonably consistent with the previous ones. We apply the same extrapolation procedure to the infinite volume limit as in Sec. II. From the fits we obtain the following binding energy for the two channels:

$$-\Delta E_\infty = \begin{cases} 7.5(0.5)(0.9)\ \mathrm{MeV} & \text{for } ^3S_1 \\ 4.4(0.6)(1.0)\ \mathrm{MeV} & \text{for } ^1S_0 \end{cases}, \qquad (18)$$

where the first and second errors are statistical and systematic. These results are reasonably consistent with the ones in Sec. II.

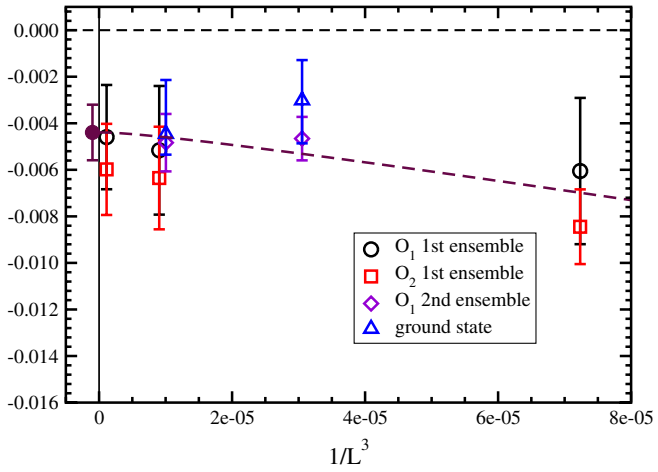

FIG. 28 (color online). Same as Fig. 27 for the $^1S_0$ channel.

IV. CONCLUSION AND DISCUSSION

We have carried out two calculations in quenched QCD to investigate whether the two-nucleon systems are bound or not at the heavier quark mass, corresponding to $m_\pi = 0.8$ GeV. In the first calculation, we have focused on the ground state of the two-nucleon system, and have investigated the volume dependence of the energy shifts obtained with two different source operators. We have found that the ground state in the $^3S_1$ channel has little volume dependence, and a finite energy shift remains in

the infinite volume limit. Based on these results we have concluded that the ground state is a bound state at the heavy quark mass. A similar result is obtained in the $^1S_0$ channel, though the binding energy is almost half of the one in the $^3S_1$ channel.

In the second calculation we have carried out a two-state analysis using the diagonalization method. The ground and first excited states are well separated on the $(6.1\ \mathrm{fm})^3$ box, and the ground-state energies for the two channels agree with the ones obtained from the single-state analysis. The energy of the first excited state is positive and far below the free two-nucleon energy with the lowest relative momentum in both channels. This leads to the conclusion that each channel has one bound state. We obtain similar results on the $(4.1\ \mathrm{fm})^3$ box, though the contaminations from higher excited states may be larger than the $(6.1\ \mathrm{fm})^3$ case. The energy of the first excited state increases as the volume diminishes. The scattering length is obtained from the energy of the first excited state using the finite volume formula. The results in the two volumes reasonably agree with each other. In the $^3S_1$ channel the scattering length is roughly one fifth of the experimental value. The difference might be attributed to the heavier quark mass employed in this calculation.

Although the results in the two-state analysis look reasonable, we ignore possible systematic error stemming from contaminations of higher excited states than the first excited state. Thus, it is an important future work to estimate the size of the systematic error using the diagonalization method with a larger correlation function matrix.

The existence of the bound state and the negative scattering length in the $^1S_0$ channel looks odd from the experimental point of view. In addition we cannot directly compare our result with those of the model calculations, which are restricted around physical quark masses. We expect that the bound state vanishes at some lighter quark mass, where the scattering length diverges, changing the sign from negative to positive. Further reduction of the quark mass would decrease the scattering length. Confirmation of this scenario requires one to investigate the quark mass dependences of the binding energy and the scattering length. We leave this study to future work.

ACKNOWLEDGMENTS

Numerical calculations for the present work have been carried out on the HA8000 cluster system at Information Technology Center of the University of Tokyo, on the PACS-CS computer under the ''Interdisciplinary Computational Science Program'' of the Center for Computational Sciences, University of Tsukuba, and on the T2K-Tsukuba cluster system at University of Tsukuba. We thank our colleagues in the PACS-CS Collaboration for helpful discussions and providing us the code used in this work. This work is supported in part by Grants-in-Aid for Scientific Research from the Ministry of Education, Culture, Sports, Science and Technology (Nos. 18104005, 18540250, and 22244018) and Grants-in-Aid of the Japanese Ministry for Scientific Research on Innovative Areas (Nos. 20105002, 21105501, and 23105708).

[1] T. Yamazaki, Y. Kuramashi, and A. Ukawa (PACS-CS Collaboration), Phys. Rev. D **81**, 111504 (2010).
[2] S. R. Beane *et al.* (NPLQCD Collaboration), Phys. Rev. D **81**, 054505 (2010).
[3] S. Beane *et al.* (NPLQCD Collaboration), Phys. Rev. Lett. **106**, 162001 (2011).
[4] T. Inoue *et al.* (HALQCD Collaboration), Phys. Rev. Lett. **106**, 162002 (2011).
[5] M. Fukugita, Y. Kuramashi, H. Mino, M. Okawa, and A. Ukawa, Phys. Rev. Lett. **73**, 2176 (1994).
[6] M. Fukugita, Y. Kuramashi, M. Okawa, H. Mino, and A. Ukawa, Phys. Rev. D **52**, 3003 (1995).
[7] S. R. Beane, P. F. Bedaque, K. Orginos, and M. J. Savage, Phys. Rev. Lett. **97**, 012001 (2006).
[8] N. Ishii, S. Aoki, and T. Hatsuda, Phys. Rev. Lett. **99**, 022001 (2007).
[9] S. Aoki, T. Hatsuda, and N. Ishii, Comp. Sci. Disc. **1**, 015009 (2008).
[10] S. Aoki, T. Hatsuda, and N. Ishii, Prog. Theor. Phys. **123**, 89 (2010).
[11] M. Lüscher, Commun. Math. Phys. **105**, 153 (1986).
[12] M. Lüscher, Nucl. Phys. **B354**, 531 (1991).
[13] M. Lüscher and U. Wolff, Nucl. Phys. **B339**, 222 (1990).
[14] S. Sasaki and T. Yamazaki, Phys. Rev. D **74**, 114507 (2006).
[15] Y. Iwasaki, Report No. UTHEP-118, 1983 (unpublished).
[16] A. Ali Khan *et al.* (*CP*-PACS Collaboration), Phys. Rev. D **65**, 054505 (2002).
[17] I. P. Omelyan, I. M. Mryglod, and R. Folk, Comput. Phys. Commun. **151**, 272 (2003).
[18] T. Takaishi and P. de Forcrand, Phys. Rev. E **73**, 036706 (2006).
[19] S. R. Beane, P. F. Bedaque, A. Parreno, and M. J. Savage, Phys. Lett. B **585**, 106 (2004).
[20] E. Epelbaum, U.-G. Meissner, and W. Gloeckle, Nucl. Phys. **A714**, 535 (2003).
[21] S. R. Beane and M. J. Savage, Nucl. Phys. **A717**, 91 (2003).
[22] V. V. Flambaum and R. B. Wiringa, Phys. Rev. C **76**, 054002 (2007).

[23] J.-W. Chen, T.-K. Lee, C. P. Liu, and Y.-S. Liu, arXiv:1012.0453.
[24] N. Ishii (PACS-CS Collaboration and HALQCD Collaboration), Proc. Sci., LAT2009 (2009) 019 [arXiv:1004.0405].
[25] M. Gockeler, H. A. Kastrup, J. Westphalen, and F. Zimmermann, Nucl. Phys. **B425**, 413 (1994).
[26] S. Aoki *et al.* (*CP*-PACS Collaboration), Phys. Rev. D **71**, 094504 (2005).
[27] K. Sasaki and N. Ishizuka, Phys. Rev. D **78**, 014511 (2008).